THE JOURNAL OF PHYSICAL CHEMISTRY C

Article

pubs.acs.org/JPCC

Mixed Phases as a Route to Self-Passivation: Effect of π-Stacking Backbone on the Physical and Electrical Properties of Naphthalenediimide Derivatives

Pramod Kumar,[†] Yulia Gerchikov,[‡] Nir Tessler,[†] and Yoav Eichen*[,‡]

[†]Department of Electrical Engineering, Nanoelectronics Center, and [‡]Schulich Faculty of Chemistry, Technion—Israel Institute of Technology, Technion City, Haifa 3200008, Israel

Supporting Information

ABSTRACT: Solution processable p- and n-type organic semiconductors are candidates for low-cost, large-area, and roll-to-roll printing of inexpensive mass-production electronics. In these organic semiconductors, it is the π-conjugated backbone that plays the major role in charge-carrier transport across the channel. In order to achieve better device performance, it is required to have better packing/crystallinity to minimize defects and avoid deep traps, so that effective transfer of charge carriers can take place in the solid state. Excellent results have been reported by blending crystal-forming organic semiconductors with amorphous polymers that serve as binders or passivating agents. We show that, for some molecular structures and processing conditions, mixtures of stereoisomers can separate and self-arrange into a thin amorphous layer covered by a polycrystalline layer. In this work, we focus on two families of constitutional isomers that differ only in the position of the pyridine groups on the π-skeleton and study the effect of the structure on the physical and electrical properties using absorption spectroscopy, AFM, X-ray, and organic field-effect transistor current−voltage response.

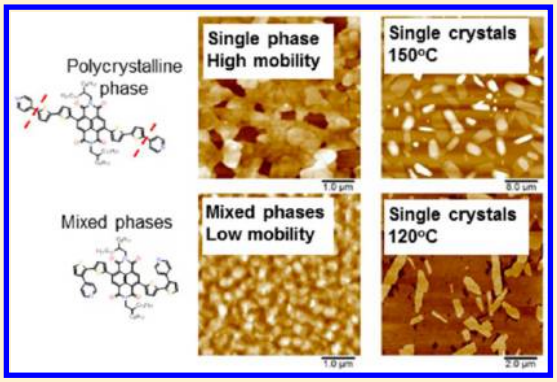

INTRODUCTION

Organic semiconductors have been studied for many years due to their potential applications in many areas, such as light-emitting diodes,[1−3] organic lasers,[4] field-effect transistors (FETs),[5,6] sensors,[7,8] and photovoltaic cells.[9,10] In these, one of the most researched areas is organic field-effect transistors (OFETs), due to their potential low production costs, large area compatibility, and potential flexibility, a desired property in flexible and wearable electronics.[11] OFETs can be either p-type (hole conductors) or n-type (electron conductors), which nowadays are both relatively easy to make. However, high-performance OFETs, especially n-type, often require surface passivation of the gate dielectric. For example, in the case of silicon oxide surface, the hydroxyl groups act as traps for electrons, leading to poor OFET performance.[12]

Solution processable organic semiconductors are of great interest for roll-to-roll deposition and low-cost production. Solution processability of small molecules is normally achieved by attaching bulky side groups to their skeleton, and the effect of various bulky groups has been widely studied.[13−18] For longer oligomers, it is observed that solution processability and crystallinity of the final film are a function of the interplay between the flatness of the π-conjugated backbone and the nature of the solubilizing groups. In both cases, solubilizing groups may hinder the π−π-stacking and thus reduce crystallinity.[19] Recently, strategies involving the blending of amorphous polymers with crystalline small molecules resulted in devices having high mobility values.[20−22] Here we report that small molecules may self-segregate into an amorphous layer covered by a polycrystalline one.

In this study, we try to minimize, as much as possible, the differences in the chemical structure so as to emphasize the role of molecular stacking and crystallization. We have used two almost identical π-backbones (constitutional isomers) having the same solubilizing groups and very similar conjugated backbones, differing only in the position where the pyridine groups are attached to the π-backbone (Figure 1a). As a result, in one system the pyridine groups are attached at a position that prevents planarization of the π-system ($\mathbf{N_{NF}}$), while in the other family (Figure 1b), the pyridine groups are connected in a way that does not cause significant steric hindrance, resulting in a flatter π-skeleton ($\mathbf{N_F}$).

We tested thin films made of $\mathbf{N_{NF}}$ and $\mathbf{N_F}$ following annealing at different temperatures inside a vacuum oven. The films made of the nonflat ($\mathbf{N_{NF}}$) molecule showed striking differences when annealed at temperatures close to the melting point. We observed a vertical phase separation where the amorphous phase passivates the SiO_2 dielectric and on top of it crystals start to grow. It was also found that if the SiO_2 was prepassivated by octadecyltrichlorosilane (OTS), the vertical

Received: June 18, 2016
Revised: September 26, 2016
Published: September 27, 2016

DOI: 10.1021/acs.jpcc.6b06175
J. Phys. Chem. C 2016, 120, 23221−23229

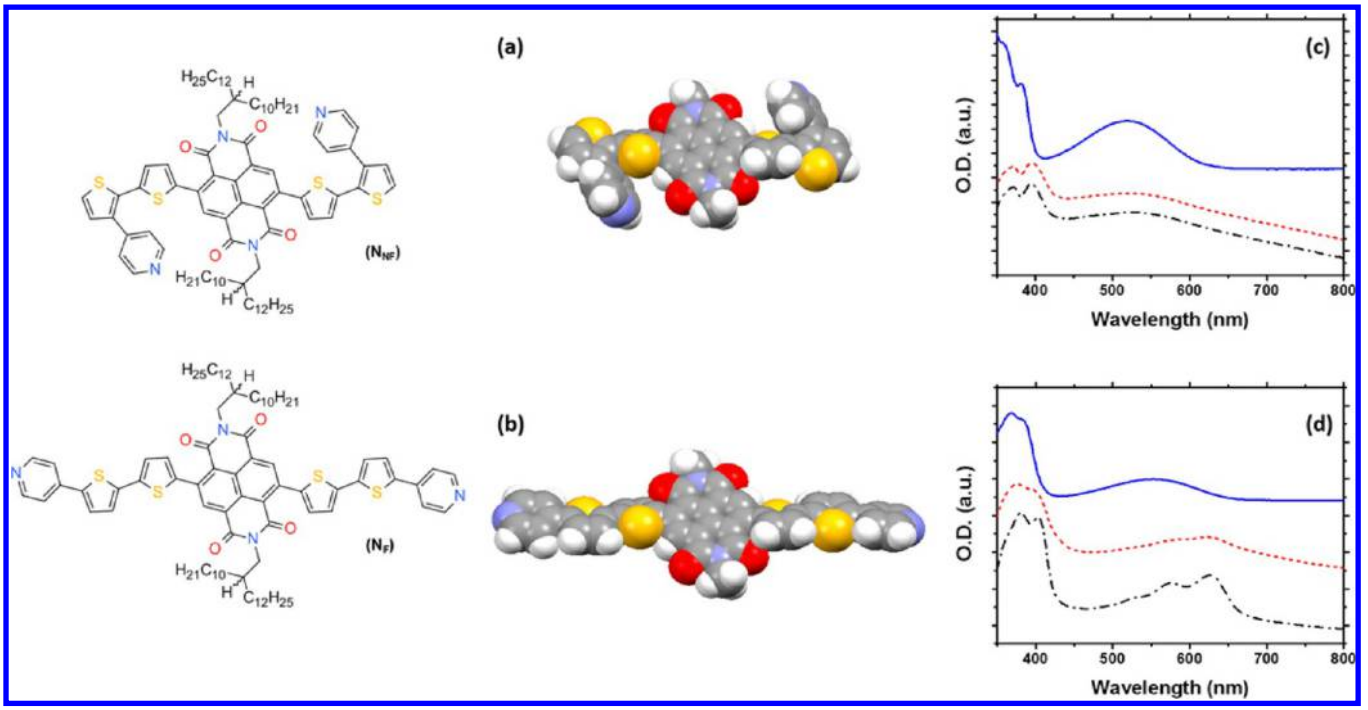

Figure 1. Energy-minimized [DFT, B3LYP/6-31G(d), alkyl groups were omitted from the drawings for clarity] structures of $\mathbf{N_{NF}}$ and $\mathbf{N_F}$, (a) showing the twisted π-conjugated backbone of $\mathbf{N_{NF}}$ and (b) the flatter backbone structure of $\mathbf{N_F}$. (c) Absorption spectra of $\mathbf{N_{NF}}$ in solution (solid blue) and films on glass substrates annealed at 30 °C (red dashed) and 100 °C (black dash-dot). (d) Absorption spectra of $\mathbf{N_F}$ in solution (solid blue) and films on glass substrates annealed at 30 °C (red dashed) and 120 °C (black dash-dot). Curves were spread vertically for clarity.

Scheme 1. Preparation of $\mathbf{N_{NF}}$[a]

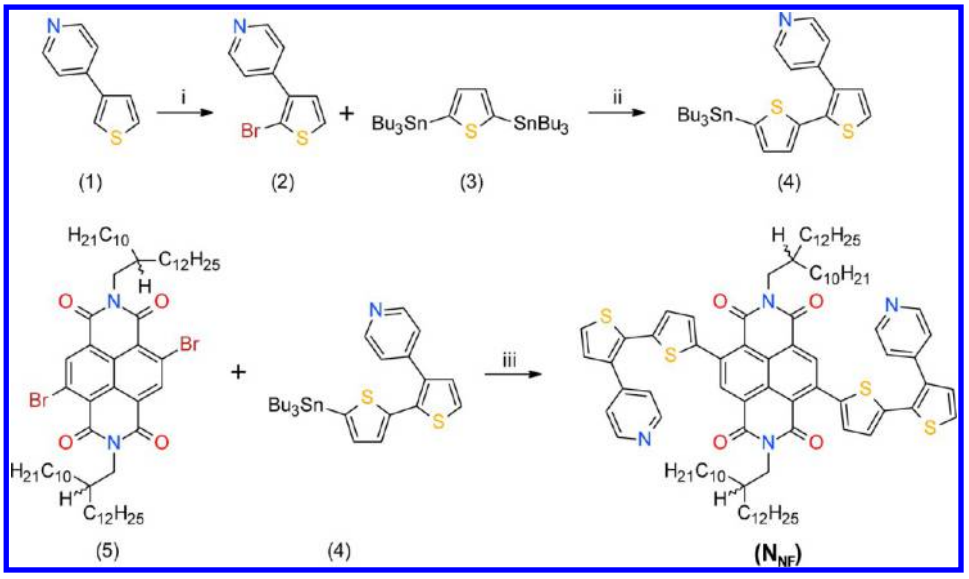

[a](i) NBS in $CH_3COOH/H_2O/CCl_4$; (ii) $Pd(PPh_3)_4$, toluene, reflux; (iii) $Pd(PPh_3)_4$, toluene, reflux.

phase separation did not occur and the molecules started directly to form single crystals, without an amorphous underlayer. The molecule with flatter backbone behaved normally with single crystal formation when annealed close to its melting temperature, both on OTS-treated and bare SiO_2 substrates.

RESULTS AND DISCUSSION

Small molecules, labeled $\mathbf{N_{NF}}$ and $\mathbf{N_F}$, were prepared according to Schemes 1 and 2, respectively. Compound **1**[8] was monobrominated using *N*-bromosuccinimide (NBS) in a mixture of solvents (H_2O/CCl_4/acetic acid, 5:1:94 v/v), affording 2-bromo-3-(4-pyridyl)thiophene (**2**) in 80% yield. Compound **4** was prepared by a Stille coupling reaction between **3** and **2**. Palladium-catalyzed cross-coupling reaction between **5**[23] and **4** afforded $\mathbf{N_{NF}}$ in 70% yield.

$\mathbf{N_F}$ was prepared in four synthetic steps. Compound **8**[24] was brominated using NBS in acetic acid, affording 4-(2-thienyl)-pyridine (**9**), in 90% yield. Compound **10** was prepared using Stille coupling between **3** and **10**. Palladium-catalyzed cross-coupling reaction between **5** and **10** afforded $\mathbf{N_F}$ in 50% yield.

DOI: 10.1021/acs.jpcc.6b06175
J. Phys. Chem. C 2016, 120, 23221−23229

Scheme 2. Preparation of N_F[a]

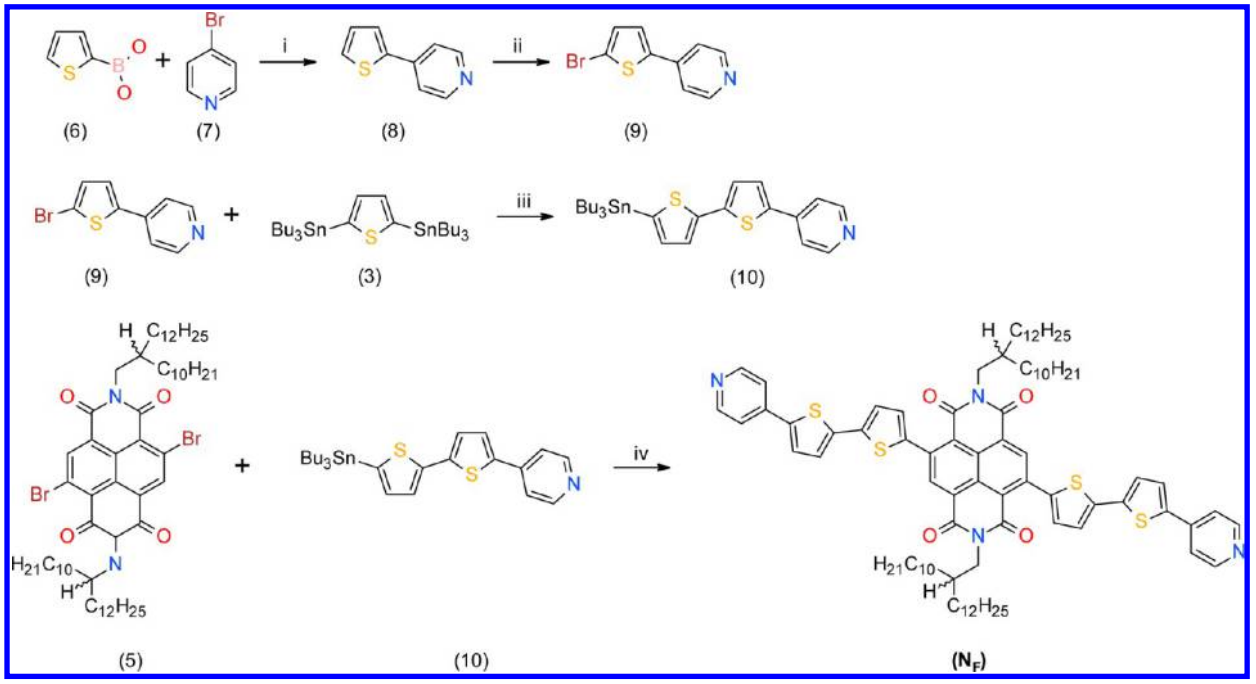

[a](i) $Pd(PPh_3)_4$, DME, Na_2CO_3; (ii) NBS in CH_3COOH; (iii) $Pd(PPh_3)_4$, toluene, reflux; (iv) $Pd(PPh_3)_4$, toluene, reflux.

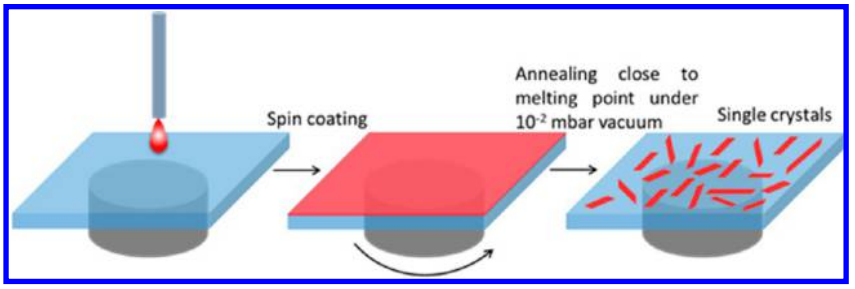

Figure 2. Schematic showing the process of growing microsized crystals on SiO_2 substrate. The molecules were first spin-coated at the required concentration and then annealed close to the melting point of the film for 1−3 h, which increased the diffusion mobility of the molecules, allowing them to self-arrange into microsized single crystals.

Figure 1a,b show the molecular structures of N_{NF} and N_F, respectively. As each of the solubilizing groups contains one chiral center, each of these new structures is composed of three isomers—*S,S* (25%), *R,R* (25%), and *S,R* (50%)—that differ in the three-dimensional organization of the groups around the two chiral atoms. The energy-minimized [DFT, B3LYP/6-31G(d)] structures of N_{NF} and N_F are presented in Figure 1, omitting the alkyl groups from the drawings for clarity, and their complete structures (both in the *S,R* structures) are presented in Figure S1 of the Supporting Information. The energy-minimized structure of N_{NF} shows that the pyridine rings induce a considerable twist of the π-conjugated backbone, resulting in a considerable restriction of its ability to flatten and π-stack This originates from the steric hindrance between the pyridine and thiophene rings, resulting in an interplanar angle of 44.1° between the pyridine and thiophene ring to which it is bound, an interplanar angle of 40.6° between the two thiophene rings, and an interplanar angle of 40° between the naphthaleneimide and the thiophene ring to which it is attached (see Figure 1). In contrast, N_F shows a considerably flatter structure, as the pyridine and thiophene rings do not form such a sterically hindered structure, resulting in an interplanar angle of 20° between the pyridine and thiophene ring to which it is bound, an interplanar angle of 20° between the two thiophene rings, and an interplanar angle of 44° between the naphthaleneimide and the thiophene ring to which it is attached (see Figure 1). The HOMO/LUMO level derivation from cyclic voltammetry (*C*−*V*) for both the molecules is given in the Supporting Information (Figures S2 and S3). For N_{NF} the HOMO/LUMO are 6.0/4.0 eV and for N_F are 5.15/3.3 eV. The elemental analysis for both the molecules is presented in the Supporting Information (Table S1).

Thin films of N_{NF} and N_F were prepared by spin-coating their solutions on bare SiO_2 gate insulating layer, on OTS-coated SiO_2 insulating layer, and on glass substrates. The fresh films were subsequently annealed at different temperatures. The resulting films were characterized using UV−vis spectroscopy, atomic force microscopy (AFM), and differential scanning calorimetry (DSC). Parts c and d of Figure 1 show absorption spectra of solutions and thin films on glass surfaces of N_{NF} and N_F, respectively, annealed well below their melting temperatures. The absorption peaks show a red shift from solution to thin films due to solid-state packing. The spectral shift and the structure appearing in the annealed films of N_F are evidence of

DOI: 10.1021/acs.jpcc.6b06175
J. Phys. Chem. C 2016, 120, 23221−23229

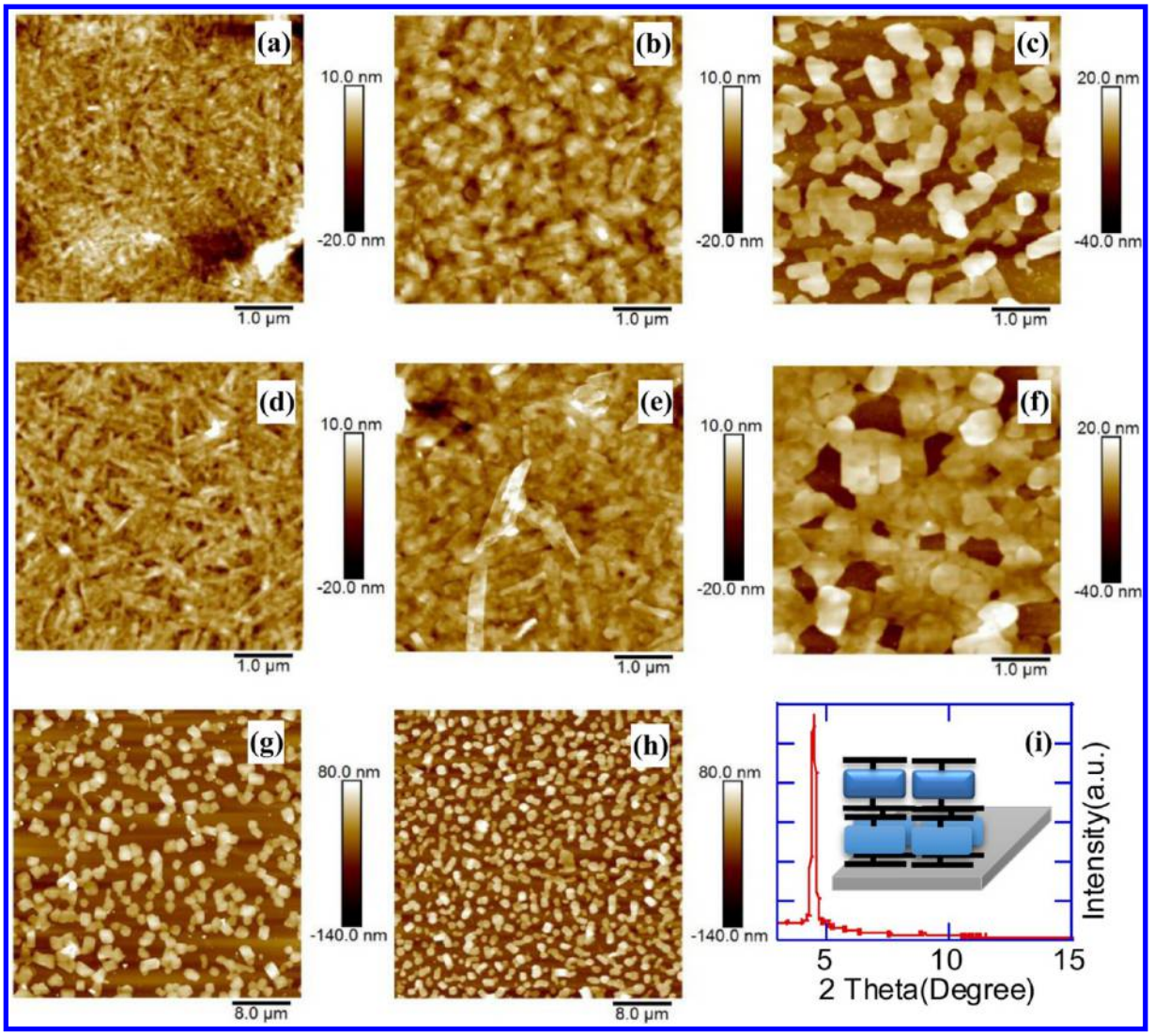

Figure 3. AFM scans of spin-coated thin films of $\mathbf{N_F}$ grown on SiO_2 (a–c, and g) and OTS-treated SiO_2 (d–f, and h) from THF solutions having concentrations of 5 mg/mL. Films were annealed at different temperatures: 60 °C (a and d), 90 °C (b and e), 120 °C (c and f), and 150 °C (g and h). (i) X-ray diffraction of $\mathbf{N_F}$ on SiO_2 substrates after annealing at 120 °C. The diffraction peaks in the case of $\mathbf{N_F}$ is the evidence of molecular packing and the inset shows the packing of $\mathbf{N_F}$.

better π–π interactions and packing as well as increased order.[19,25−27] The absence of this phenomenon in $\mathbf{N_{NF}}$ can be attributed to the hindered stacking caused by the nonplanar π-skeleton. This leads to less-ordered molecular packing and to the amorphous nature of the resulting thin films of $\mathbf{N_{NF}}$.

To gain more insight into the morphological and packing differences between films made from these two oligomers, we prepared films on various substrates and annealed them at temperatures close to (below) their melting points. Annealing close to the melting point temperature was found to be a good method for growing single crystals. DSC measurements to determine melting points for both $\mathbf{N_{NF}}$ and $\mathbf{N_F}$ are shown in Figure S4 of the Supporting Information. The growth of crystals at temperatures close to the melting point are shown in Figures S5 and S6 of the Supporting Information. The process of spin-coating and annealing, close to the melting point, under reduced pressure (10^{-2} mbar) for 1–3 h, to form single crystals is shown schematically in Figure 2.

We first present results for the $\mathbf{N_F}$ molecule, which has a relatively flat backbone. Figure 3 shows the morphologies of $\mathbf{N_F}$ films spin-coated from a 5 mg/mL solution of $\mathbf{N_F}$ in THF on SiO_2 and OTS-treated SiO_2 substrates and annealed at different temperatures (60, 90, 120, and 150 °C). The films on SiO_2 are shown in Figure 3a–c and on OTS-treated SiO_2 are shown in Figure 3d–f. One can see a marked change in film morphologies with temperatures where annealing at higher temperatures shows growth of larger crystalline grains. For the temperature close to the melting point (150 °C), the growth of single crystallites is observed (Figure 3, part g for SiO_2 and part h for OTS-treated SiO_2). Figure 3i shows the XRD pattern of the crystals and the proposed resulting model for the packing of the molecules. The XRD pattern fits to packing having a periodicity of 1.97 nm, which suggests that $\mathbf{N_F}$ molecules self-assemble with their π-skeleton perpendicular to the plane of the substrate. Thin film XRD measurements are given in Figure S7a of the Supporting Information, which show single phase development after 60 °C.

Next, we studied the twisted molecule, $\mathbf{N_{NF}}$. The AFM images in Figure 4a–d show films of $\mathbf{N_{NF}}$ (spin-coated from a 5 mg/mL solution of $\mathbf{N_{NF}}$ in THF) on SiO_2 substrates following

DOI: 10.1021/acs.jpcc.6b06175
J. Phys. Chem. C 2016, 120, 23221−23229

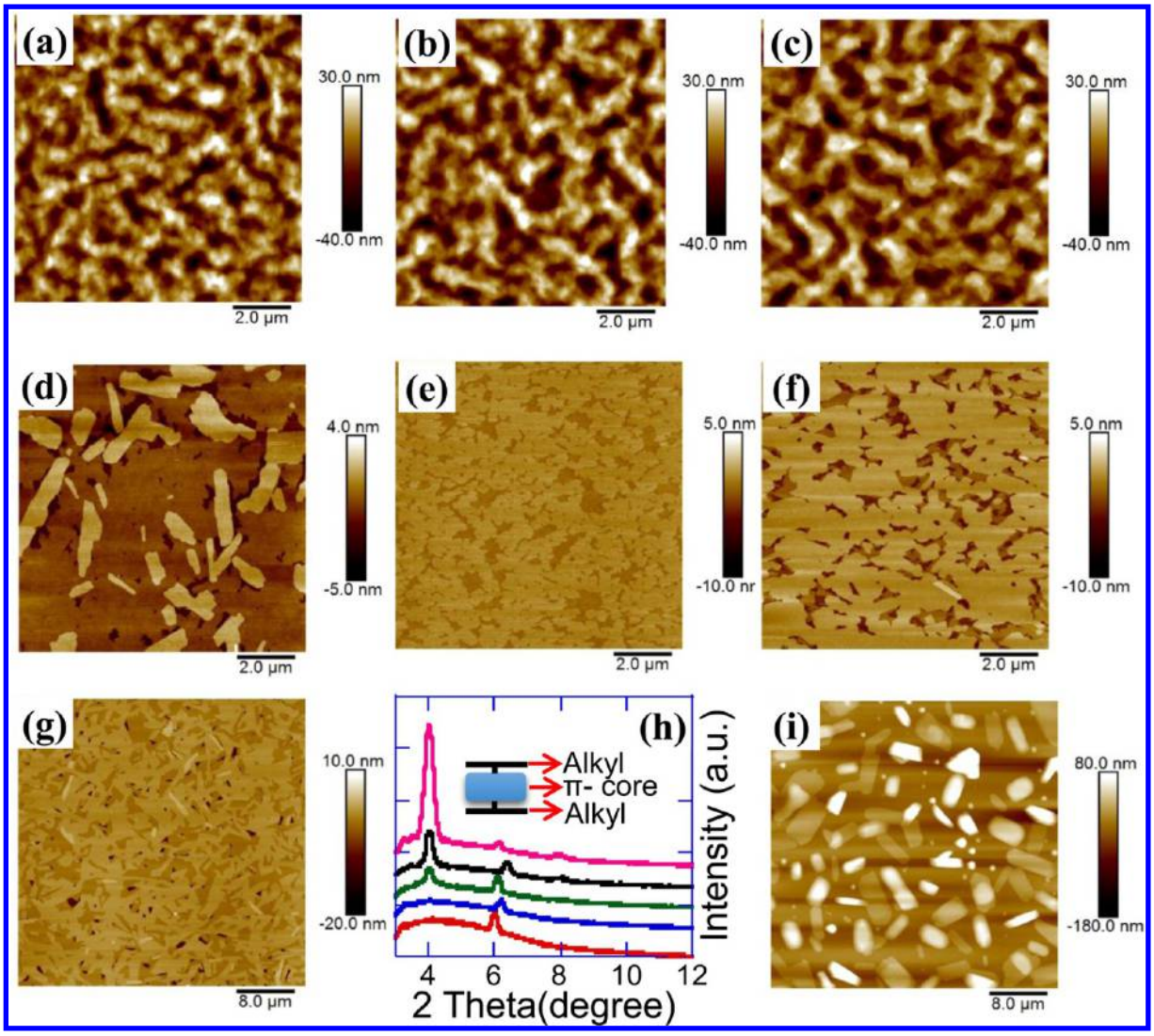

Figure 4. AFM scans of spin-coated thin films of N_{NF} grown on SiO_2 (a–g) and OTS-treated SiO_2 (i). Parts a–d and i were spin-coated from 5 mg/mL THF solutions and annealed at 60 °C (a), 90 °C (b), 110 °C (c), and 120 °C (d, i). Parts e–g were all annealed at 120 °C, but the source solution concentrations were 0.5 mg/mL (d), 1 mg/mL (e), and 2 mg/mL (f). Part h shows that X-ray diffraction of N_{NF} films prepared at different concentrations shifted upward (0.5, 1, 2, 4, 5 mg/mL) on SiO_2 substrates after annealing at 120 °C. The diffraction peaks from films of 0.5 and 1 mg/mL solutions show packing of the lower layer which is different from that of the top crystals. The top layer of crystals starts to show via X-ray at 2 mg/mL and increase in intensity.

annealing at different temperatures under reduced pressure (10^{-3} mbar). It was found that films annealed at temperatures up to 110 °C (Figure 4a–c) do not show crystal formation, while those annealed at 120 °C, which is close to the melting temperature, show clear crystal formation (Figure 4d). We attribute the lack of crystal formation, below the melting point, to the protruding pyridine groups that make it more difficult to π-stack and thus hinder crystal formation. These protruding pyridine groups of N_{NF} require very specific orientation in order for the attractive forces to come into play and form crystals. To overcome this effective barrier, a higher temperature is needed so that the molecular motion is enhanced, which simultaneously also enhances the mobility of the molecules on the surface, allowing them to better organize. A similar phenomenon of hindered packing and crystallization was also reported for rubrene.[28−31] The reason put forward was the twisted phenyl groups connected to the tetracene backbone of the molecule, which hinder the crystalline packing and hence promote amorphous−polycrystalline growth. For vapor-phase-deposited molecules, this amorphous−polycrystalline growth could be avoided using a high deposition rate, which was shown to lead to single crystals and high charge carrier mobility.[32,33]

Crystallization is a complex interplay between nucleation and crystal growth.[34] In our case, both N_{NF} and N_F are crystalline under the appropriate conditions. It is thus suggested that the crystal packing of N_{NF} is less accessible than that of N_F, due to the fact that in such low-symmetry and bulky systems most of the possible relative orientations of the two molecules generate repulsive interactions. In such cases, one would expect the formation of more nucleation sites and less crystal growth. In flatter systems, such as N_F, there are more relative orientations that yield attractive interactions that funnel the system eventually to the formation of crystals.

Annealing at 120 °C, which is close to the melting temperatures of both systems, yields clear crystal formation (Figure 4d). Looking more closely at the AFM picture, we note that there are two layers. The bottom one looks continuous and

DOI: 10.1021/acs.jpcc.6b06175
J. Phys. Chem. C 2016, 120, 23221−23229

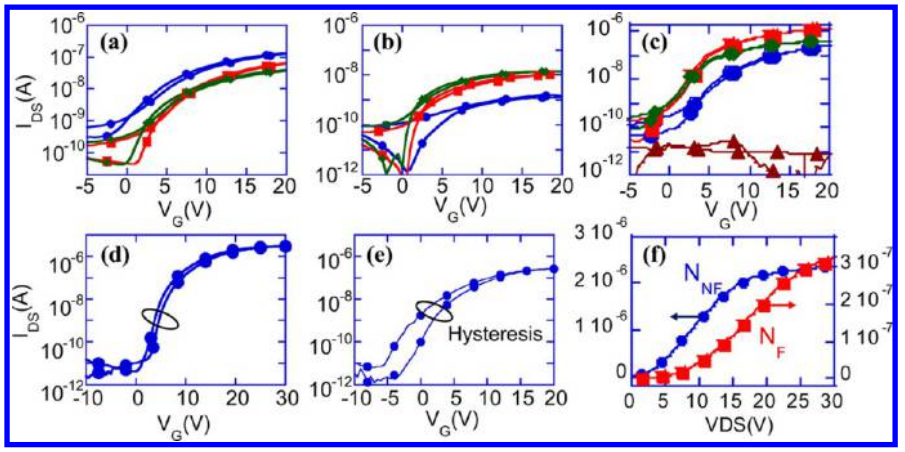

Figure 5. Transfer characteristics at V_{DS} = 15 V of (a) $\mathbf{N_{NF}}$ OFETs, where thin films on bare SiO_2 were annealed at 60 °C (circles), 90 °C (squares), and 110 °C (diamonds); (b) $\mathbf{N_F}$ OFETs, where thin films on bare SiO_2 were annealed at 60 °C (circles), 90 °C (squares), and 120 °C (diamonds); (c) same as part b ($\mathbf{N_F}$ OFETs) but on OTS-treated SiO_2; (d and e) transfer characteristics of single-crystal devices on bare SiO_2 for $\mathbf{N_{NF}}$ and $\mathbf{N_F}$, respectively. (f) Normalized (W/L) output characteristics at V_G = 20 V for the single-crystal FETs made of $\mathbf{N_{NF}}$ and $\mathbf{N_F}$.

lacks structure, almost fully covering the surface, while the upper one is faceted and discontinuous.

To better understand the two layers (see also Figure S8 in the Supporting Information), we examined films annealed at 120 °C but coated from solutions having different concentrations of $\mathbf{N_{NF}}$. Figure 4e,f,g shows results obtained from films coated from 0.5, 1, and 2 mg/mL solutions of $\mathbf{N_{NF}}$ in THF, respectively. Moving from a concentration of 0.5 mg/mL (Figure 4e) to 1 and 2 mg/mL, we note that the lower layer does not seem to change while the upper layer develops clear facets (Figure 4g). The even larger crystals shown in Figure 4d are thus in direct correlation with the higher concentration used (5 mg/mL). Figure 4h shows the XRD pattern of 0.5, 1, 2, 4, and 5 mg/mL films. The results were shifted upward starting with 0.5 mg/mL at the bottom and up to 5 mg/mL. The peak at ∼4° grows with the concentration used and becomes significant at 5 mg/mL. Similar molecular packing (see also the inset to Figure 3i) was reported for other molecules as well.[35,36] Here $\mathbf{N_{NF}}$ self-arranges with its π-skeleton perpendicular to the plane of the substrate with ∼2.2 nm spacing.

The small peak at ∼6° is attributed to the underlayer, which remains largely amorphous. The formation of a thin wetting layer is a known phenomenon which, in the context of organic molecules, was reported for vapor-phase growth of pentacene on SiO_2.[37−39] In the case of pentacene, it was reported that the first few monolayers are different from the crystalline structure formed above them and this was attributed to the relative strength of the interaction between the molecules, which would promote edge-on formation, and the interaction with the SiO_2, which would promote a face-on one.[38] Lastly, we performed a similar annealing process but on OTS-treated SiO_2 substrate (Figure 4i). Figure 4i shows a growth pattern that is completely different from the one on SiO_2 substrate untreated with OTS. It shows microsized single crystals and the absence of the self-passivating layer. This is in line with the suggestion that the wetting layer formation would be due to the SiO_2 interface interaction that promotes face-on molecular orientation.[38] Thin film XRD measurements are given in the Supporting Information (Figure S7b), which shows multiple phase development above 60 °C.

As Figures 3 and 4 show, there is an effect of crystal formation with ($\mathbf{N_{NF}}$) or without ($\mathbf{N_F}$) a passivation underlayer, and on top of it, there is the effect of interconnectivity between the crystals. Indeed, when we measure OFETs made of films, it is difficult to separate the effects. Figure 5a shows the performance of OFETs based on films of $\mathbf{N_{NF}}$ annealed at temperatures of 60 °C (circles), 90 °C (squares), and 110 °C (diamonds). These correspond to Figure 4, parts a, b, and c, respectively. Figure 5b shows the performance of OFETs based on films of $\mathbf{N_F}$ annealed at temperatures of 60 °C (circles), 90 °C (squares), and 120 °C (diamonds). These correspond to Figure 3, parts a, b, and c. The slight differences between devices made of films of the different molecules is that the current (mobility) for $\mathbf{N_{NF}}$ is slightly higher compared to that of $\mathbf{N_F}$ and that annealing clearly enhances the performance of transistors based on $\mathbf{N_F}$, while for $\mathbf{N_{NF}}$ the on/off current increases but the on current decreases. The situation may be even more confusing when examining films on OTS. For the case of $\mathbf{N_{NF}}$, there is not much difference in the performance of the OFETs (not shown), but for the $\mathbf{N_F}$-based OFETs, the performance is enhanced drastically (see Figure 5c).

To isolate the role of the passivating underlayer of the $\mathbf{N_F}$ molecule, we tested single-crystal OFETs. Single-crystal FETs were prepared, for both molecules, on prepatterned source-drain electrodes by spin-coating low-concentration solutions to get fewer crystals that can develop between the source and drain electrodes. The OFETs performance are shown in Figure 5, parts d ($\mathbf{N_{NF}}$) and e ($\mathbf{N_F}$). The extracted charge-carrier mobility for the single-crystal transistors was on the order of 0.1 and 0.01 $cm^2/(V\ s)$ for the $\mathbf{N_{NF}}$- and $\mathbf{N_F}$-based transistors, respectively. Also the $\mathbf{N_F}$-based OFET exhibits hysteresis, while the $\mathbf{N_{NF}}$-based OFET is hysteresis free. It is known that the OH at the SiO_2 interface serves as an electron trap, which degrades the performance of FETs.[12] Hence, we attribute the differences, in mobility and hysteresis, to the fact that crystals of $\mathbf{N_{NF}}$ develop on an amorphous passivating layer that separates them from the SiO_2 substrates, as seen in Figure 4e, while crystals of $\mathbf{N_F}$ grow on bare SiO_2, without any passivating layer, as seen in Figure 3g. Figure 5f compares the normalized (W/L) output characteristics (I_{DS}−V_{DS}) at V_G = 20 V for single-crystal transistors, where $\mathbf{N_F}$ shows less current than $\mathbf{N_{NF}}$ in single-crystal OFETs. The values of charge carrier mobility in OTFTs and single-crystal transistors are summarized in Table 1, in which $\mathbf{N_{NF}}$ OTFTs show no improvement with annealing temperatures due to the presence of mixed phases, whereas $\mathbf{N_F}$ OTFTs show improvement due to higher ordering, as shown in

DOI: 10.1021/acs.jpcc.6b06175
J. Phys. Chem. C 2016, 120, 23221−23229

Table 1. Charge Carrier Mobility Obtained in Thin Films and Single Crystal Transistors

	mobility ($cm^2/(V\ s)$)	
temp (°C)	N_{NF}	N_F
60	6.1×10^{-5}	1.5×10^{-5}
90	5.3×10^{-5}	1.0×10^{-3}
110	5.9×10^{-5}	–
120	–	3.7×10^{-4}
single crystal	0.1	0.01

the rise of the XRD peak in Figure S7 of the Supporting Information .

CONCLUSIONS

In summary, two families of constitutional isomers that differ mainly in the flatness of their π-conjugated backbone exhibit very different morphological, crystal-forming, and physical properties. In our case, it is the position where two pyridine rings are attached to the π-backbone that leads to differences in the tendency of the molecules to form the crystal structure. The oligomer with a flatter π-skeleton self-arranges better due to the simpler route to crystallinity, giving rise to polycrystalline films, the morphology of which can be tuned through the annealing temperatures. The oligomer with twisted protruding groups shows changes in the polycrystalline state only at temperatures close to its melting point. The interesting phenomena discovered is of self-passivation, where substrate interaction leads to vertical phase separation of a relatively amorphous thin film of ~5 nm covered by a polycrystalline structure. The self-passivating initial layer of $\mathbf{N_{NF}}$ developed on SiO_2 but not on OTS-treated SiO_2 substrates. The effect of the passivation layer can be isolated when measuring a single-crystal OFET on SiO_2; however, the very different contact barrier (Figure 5f) makes it less clear-cut. To minimize the effect of the contact barrier, we deduced the mobility at high V_{DS} and found that the $\mathbf{N_F}$ molecules shows a mobility of ~0.01 $cm^2/(V\ s)$, where the crystal with less $\pi-\pi$-stacking ability ($\mathbf{N_{NF}}$) exhibited an order of magnitude higher mobility. We attribute this difference, at least in part, to the passivation layer. In the case of polycrystalline films, $\mathbf{N_{NF}}$ showed poorer performance due to reduced connectivity between the crystals. We believe that further study will show how to enhance chemically both the self-passivation phenomena and the crystalline interconnectivity.

EXPERIMENTAL METHODS

Apparatus. *Films and Device Fabrication.* Solutions of $\mathbf{N_{NF}}$ and $\mathbf{N_F}$ were prepared in THF and then spin-coated (2000 rpm for 60 s) onto glass substrates for optical measurements while they were coated onto n++Si/SiO_2(100 nm) substrates for AFM measurements and OFETs. Films were annealed at different temperatures for studying different morphologies under rough vacuum (10^{-3} mbar). Single-crystal devices were fabricated on already patterned gold n++Si/SiO_2 substrates; the pattering was done by a photolithography technique. Solution (1–5 mg/mL) was printed on the desired area and then annealed at temperatures close to the melting point (120 °C for $\mathbf{N_{NF}}$ and 150 °C for $\mathbf{N_F}$) for 3 h in rough vacuum (10^{-3} mbar).

Measurements. NMR spectra were recorded on Bruker-AM-300 and Bruker-AM-500 spectrometers. Mass spectra were recorded using MALDI micro MX (MICROMASS) and TSQ-70B (FINNIGAN MAT) instruments. Melting points were recorded on a PL-DSC (Polymer Laboratories) machine. Optical absorption spectra of solution (in THF) and films were measured with a UV–visible–NIR spectrophotometer (UV-3101PC Shimadzu). Grazing-angle X-ray was used to measure X-ray diffraction (XRD) with the RikaguSmartLab high-resolution diffraction system. A surface profiler (Dektak 150) was used to measure the thickness of films. Their surface morphologies were measured with an atomic force microscope (AFM) system (NanoscopeIIIa, Digital Instruments). OFET measurements were done under inert atmosphere by an Agilent 1500A Semiconductor Device Analyzer.

Materials. All the starting materials and solvents described in the paper were purchased from Sigma-Aldrich and Fluka. Solvents and starting materials were used as received unless noted. Anhydrous solvents were obtained using standard methods.

*4-(2-Bromo-3-thienyl)pyridine (**2**).* *N*-Bromosuccinimide (NBS) (4 g, 22.4 mmol) was dissolved in a nonhomogenous solution of H_2O (5 mL), acetic acid (1.5 mL), and CCl_4 (84 mL). The reaction mixture was then cooled to 3–5 °C and thiophen-3-ylpyridine (**1**) (4 g, 6.8 mmol) was added in one portion. The reaction mixture was stirred at room temperature and monitored using TLC (silica, 70:30 v/v hexane:ethyl acetate). After 2 h the reaction was completed, and the mixture was cooled in an ice bath and neutralized to pH 8–9 using a saturated solution of sodium carbonate. The resulting solution was washed with dichloromethane (3 × 100 mL), and the combined organic layers were dried over sodium sulfate, filtered, and concentrated. The crude product was purified using column chromatography (silica, 70:30 v/v hexane:ethyl acetate), affording 4-(2-bromo-3-thienyl)pyridine, as a yellow solid (1.3 g, 80%).

Mp: 57 °C. ^{1}H NMR (300 MHz, $CDCl_3$): δ 8.66 (d, 2H), 7.48 (d, 2H), 7.34 (d, 1H), 7.04 (d, 1H). ^{13}C NMR (125 MHz, $CDCl_3$): δ 150.47, 142.13, 138.47, 129.39, 128.92, 123.33, 110.46. MS (MALDI) *m*/*z*: calcd for C_9H_7BrNS $[M + H]^+$ 239.94825, found 239.95.

*Tributyl[5-[3-(4-pyridyl)-2-thienyl]-2-thienyl]stannane (**4**).* 2,5-Bis(tributyltin)thiophene (2.75 g, 4.16 mmol) and Pd-$(PPh_3)_4$ (0.12 g, 0.1 mmol) were dissolved in toluene (50 mL) in an inert atmosphere. The reaction mixture was heated to reflux. Compound **2** (0.5 g, 2.08 mmol) was dissolved in toluene (50 mL) and added dropwise to the reaction mixture, and the progress of the reaction was monitored using TLC (silica, 30:70 v/v ethyl acetate:hexane). After the disappearance of the starting material (**2**), the solvent was evaporated and the crude product was purified using column chromatography (silica, 30:70 v/v ethyl acetate:hexane). Compound **4** was obtained as a yellow oil in 75% yield (0.4 g).

^{1}H NMR (400 MHz, $CDCl_3$): δ 8.46 (d, 2H), 7.27 (d, 1H), 7.2 (d, 2H) 7.05 (d, 1H), 6.89 (d, 2H), 1.56 (m, 6H), 1.27 (m, 6H), 1.18 (t, 6H), 0.84 (t, 9H). ^{13}C NMR (400 MHz, $CDCl_3$): δ 148.97, 143.13, 135.14, 133.22, 132.25, 128.48, 126.89, 128.7, 124.54, 122.93, 27.25, 25.94, 16.34, 12.57. MS (MALDI) *m*/*z*: calcd for $C_{25}H_{34}NS_2Sn$ $[M + H]^+$ 532.11546, found 532.13.

*2,6-Dibromo-N,N′-bis(2-octyldodecyl)-1,4,5,8-naphthalenedicarboximide (**5**).* Compound **5** was synthesized according to a previously reported procedure.[19]

Mp: 94 °C. ^{1}H NMR (300 MHz, $CDCl_3$): δ 8.97 (s, 2H), 4.13 (m, 4H), 1.97 (m, 2H), 1.21 (m, 80H), 0.85 (m, 12H). ^{13}C NMR (100 MHz, $CDCl_3$): δ 161.39, 161.24, 139.38, 128.59, 127.97, 125.5, 124.3, 45.67, 36.68, 32.15, 31.77, 30.25,

DOI: 10.1021/acs.jpcc.6b06175
J. Phys. Chem. C 2016, 120, 23221–23229

29.82, 29.67, 29.59, 29.57, 26.55, 22.92, 14.35. HRMS (APCI) m/z: calcd for $C_{62}H_{101}Br_2N_2O_4$ $[M + H]^+$ 1097.61079, found 1097.5985.

N,N′-Bis(2-octyldodecyl)-1,4,5,8-naphthalenedicarboximide-2,6-diyl]-alt-5,5′-(2,2′-bithiophene-4-pyridyl) (N_{NF}). Compounds **5** (0.3 g, 0.28 mmol) and **4** (0.57 g, 1.5 mmol) and $Pd(PPh_3)_4$ (0.032 g, 0.02 mmol) were dissolved in dry toluene (20 mL) under an inert atmosphere. The mixture was refluxed for 24 h and then cooled to room temperature and concentrated under reduced pressure. The crude was purified using column chromatography (silica, 30:70 v/v ethyl acetate:hexane), affording $\mathbf{N_{NF}}$, as a dark purple solid (0.3 g, 70%).

Mp: 120 °C. ^{1}H NMR (300 MHz, $CDCl_3$, TMS, 25 °C): δ 8.7 (s, 2H), 8.59 (d, 4H), 7.38 (d, 4H), 7.15 (t, 4H), 7.01 (d, 4H), 4.05 (d, 4H), 1.9 (m, 2H), 1.17 (br, 40H), 0.87 (m, 6H). ^{13}C NMR (126 MHz, $CDCl_3$): δ 162.47, 150.05, 143.77, 141.95, 139.13, 138.03, 136.62, 132.60, 129.77, 128.89, 127.47, 125.59, 123.83, 122.93, 31.88, 30.02, 29.61, 29.31, 26.64, 22.65, 14.10. HRMS (APPI) m/z: calcd for $C_{88}H_{117}N_4O_4S_4$ $[M + H]^+$ 1421.79579, found 1421.7970.

*4-(2-Thienyl)pyridine (**8**).* 4-Bromopyridine hydrochloride (**7**) (3.99 g, 20.5 mmol) and $Pd(PPh_3)_4$ (0.44 g, 0.4 mmol) were dissolved in DMF (40 mL). A solution of 2-thiopheneboronic acid (**6**) (2.62 g, 20.5 mmol) in aqueous carbonate (1 M, 45 mL) was added dropwise to the DMF solution over 20 min. After the addition, the reaction mixture was heated to reflux for 24 h, and then the reaction mixture was poured on ice−water, mixed with ether, and vigorously stirred. The aqueous phase was separated and extracted with a large volume of ether. The combined organic phases were concentrated to 20% of their initial volume and extracted with a dilute acidic aqueous solution (0.5 N HCl, 4 × 50 mL). The combined acidic aqueous extracts were filtered and neutralized, and the crude phase was extracted with three portions of ether. The combined organic phases were washed with H_2O, dried over $MgSO_4$, and concentrated, affording **8** as a white solid (2.96 g, 90%).

Mp: 80 °C. ^{1}H NMR (400 MHz, $CDCl_3$): δ 8.5 (d, 2H), 7.63 (dd, 1H), 7.43 (d, 2H), 7.34 (d, 1H), 7.07 (t, 1H). ^{13}C NMR (100 MHz, $CDCl_3$): δ 150.34, 141.44, 132.25, 128.57, 128.46, 127.25, 125.33, 119.92. MS (MALDI) m/z: calcd for C_9H_8NS 162.03774 $[M + H]^+$, found 161.87.

*4-(5-Bromo-2-thienyl)pyridine (**9**).* A mixture of **8** (2 g, 12.5 mmol) and NBS (5.5 g, 30 mmol) in acetic acid (200 mL) was stirred overnight at room temperature. The mixture was then poured on ice, made slightly basic, and extracted with three portions of dichloromethane. The combined organic layers were dried over anhydrous Na_2SO_4, filtered, and concentrated. The crude product was purified using column chromatography (silica, 75:25 v/v hexane:ethyl acetate), affording 4-(5-bromo-2-thienyl)pyridine (**9**) as a white solid (2.6 g, 90%).

Mp: 146 °C. ^{1}H NMR (300 MHz, $CDCl_3$): δ 8.6 (d, 2H), 7.39 (d, 1H), 7.26 (d, 1H), 7.08 (d, 1H). ^{13}C NMR (100 MHz, $CDCl_3$): δ 150.44, 142.62, 131.41, 125.98, 119.51. MS (MALDI) m/z: calcd for C_9H_7BrNS $[M + H]^+$ 239.94825, found 239.95.

*Tributyl[5-[5-(4-pyridyl)-2-thienyl]-2-thienyl]stannane (**10**).* 2,5-Bis(tributyltin)thiophene (**3**) (4.37 g, 6.6 mmol) and $Pd(PPh_3)_4$ (0.04 g, 0.03 mmol) were dissolved in toluene (50 mL), and the reaction mixture was heated to reflux. Compound **9** (0.8 g, 3.3 mmol) was dissolved in toluene (50 mL) and added dropwise to the reaction mixture. The progress of the reaction was monitored by TLC (silica, 30:70 v/v ethyl acetate:hexane). After the disappearance of the starting material (**9**), the solvent was evaporated and the crude product was purified using column chromatography (silica, 30:70 v/v ethyl acetate:hexane). Compound **10** was obtained as a yellow oil in 60% yield.

^{1}H NMR (400 MHz, $CDCl_3$): δ 8.56 (d, 2H), 7.42 (dd, 3H), 7.34 (d, 1H), 7.16 (d, 2H) 7.08 (d, 1H), 1.53 (m,6H), 1.34 (m, 6H), 1.18 (t, 6H), 0.84 (t, 9H). ^{13}C NMR (400 MHz, $CDCl_3$): δ 148.85, 142.95, 135.10, 133.61, 132.41, 128.48, 126.5, 126.48, 125.65, 124.33, 122.77, 27.25, 25.75, 21.63, 16.35, 13.1, 12.57. MS (MALDI) m/z: calcd for $C_{25}H_{35}NS_2Sn$ 533.12328 $[M]^+$, found 533.55.

N,N′-Bis(2-octyldodecyl)-1,4,5,8-naphthalenedicarboximide-2,6-diyl]-alt-5,5′-(2,2′-bithiophene-2-pyridyl) (N_F). Compounds **5** (0.2 g, 0.18 mmol) and **10** (0.19 g, 0.36 mmol) and $Pd(PPh_3)_4$ (0.0025 g, 0.0018 mmol) were dissolved in dry toluene (10 mL) and kept under a positive pressure of argon. The mixture was refluxed for 3 h and then cooled to room temperature and concentrated under reduced pressure. The crude product was purified using column chromatography (silica, 30:70 v/v ethyl acetate:hexane), affording $\mathbf{N_F}$, as a dark violet solid (0.13 g, 50%).

Mp: 160 °C. ^{1}H NMR (500 MHz, $CDCl_3$): δ 8.83 (s, 1H), 8.65 (d, 1H), 7.51 (dd, 1H), 7.39−7.30 (m, 1H), 4.13 (d, 1H), 2.00 (s, 1H), 1.45−1.09 (m, 22H), 0.98−0.79 (m, 3H). ^{13}C NMR (126 MHz, $CDCl_3$): δ 162.45, 162.42, 150.42, 140.86, 140.25, 139.77, 139.21, 138.52, 129.92, 127.57, 126.24, 125.47, 125.39, 124.63, 122.85, 119.48, 77.23, 76.97, 76.72, 36.51, 31.88, 31.55, 30.06, 29.67, 29.65, 29.62, 29.32, 26.35, 22.65, 14.09, 0.98. HRMS (APPI) m/z: calcd for $C_{88}H_{117}N_4O_4S_4$ $[M + H]^+$ 1421.79579, found 1421.7932.

■ ASSOCIATED CONTENT

Ⓢ Supporting Information

The Supporting Information is available free of charge on the ACS Publications website at DOI: 10.1021/acs.jpcc.6b06175.

Full energy minimized structures, DSC measurement for melting point measurement, thin film morphology and single crystal AFM, $C-V$ measurements for HOMO/LUMO calculations, and elemental analysis for both the molecules are given (PDF)

■ AUTHOR INFORMATION

Corresponding Author

*E-mail: chryoav@tx.technion.ac.il. Phone: +972-4-8293708.

Notes

The authors declare no competing financial interest.

■ ACKNOWLEDGMENTS

This work was financially supported by the Technion funds for security research.

■ REFERENCES

(1) Tang, C. W.; VanSlyke, S. A. Organic Electroluminescent Diodes. *Appl. Phys. Lett.* **1987**, *51*, 913−915.

(2) Li, N.; Oida, S.; Tulevski, G. S.; Han, S.-J.; Hannon, J. B.; Sadana, D. K.; Chen, T.-C. Efficient and Bright Organic Light-Emitting Diodes on Single-Layer Graphene Electrodes. *Nat. Commun.* **2013**, *4*, 2294.

(3) Burroughes, J. H.; Bradley, D. D. C.; Brown, A. R.; Marks, R. N.; Mackay, K.; Friend, R. H.; Burns, P. L.; Holmes, A. B. Light-Emitting-Diodes Based on Conjugated Polymers. *Nature* **1990**, *347*, 539−541.

DOI: 10.1021/acs.jpcc.6b06175
J. Phys. Chem. C 2016, 120, 23221−23229

(4) Tessler, N. Lasers Based on Semiconducting Organic Materials. *Adv. Mater.* **1999**, *11*, 363−370.
(5) Ben-Sasson, A. J.; Tessler, N. Unraveling the Physics of Vertical Organic Field Effect Transistors through Nanoscale Engineering of a Self-Assembled Transparent Electrode. *Nano Lett.* **2012**, *12*, 4729−4733.
(6) Sirringhaus, H. 25th Anniversary Article: Organic Field-Effect Transistors: The Path Beyond Amorphous Silicon. *Adv. Mater.* **2014**, *26*, 1319−1335.
(7) Gerchikov, Y.; et al. Detection of Alkylating Agents Using Electrical and Mechanical Means. *Journal of Physics: Conference Series* **2011**, *307*, 012020.
(8) Gannot, Y.; Hertzog-Ronen, C.; Tessler, N.; Eichen, Y. Sensing of Alkylating Agents Using Organic Field-Effect Transistors. *Adv. Funct. Mater.* **2010**, *20*, 105−110.
(9) Dudhe, R. S.; Sinha, J.; Kumar, A.; Rao, V. R. Polymer Composite-Based Ofet Sensor with Improved Sensitivity Towards Nitro Based Explosive Vapors. *Sens. Actuators, B* **2010**, *148*, 158−165.
(10) Tessler, N. Adding 0.2 V to the Open Circuit Voltage of Organic Solar Cells by Enhancing the Built-in Potential. *J. Appl. Phys.* **2015**, *118*, 215501.
(11) Arias, A. C.; MacKenzie, J. D.; McCulloch, I.; Rivnay, J.; Salleo, A. Materials and Applications for Large Area Electronics: Solution-Based Approaches. *Chem. Rev.* **2010**, *110*, 3−24.
(12) Chua, L. L.; Zaumseil, J.; Chang, J. F.; Ou, E. C. W.; Ho, P. K. H.; Sirringhaus, H.; Friend, R. H. General Observation of N-Type Field-Effect Behaviour in Organic Semiconductors. *Nature* **2005**, *434*, 194−199.
(13) Zerdan, R. B.; Shewmon, N. T.; Zhu, Y.; Mudrick, J. P.; Chesney, K. J.; Xue, J.; Castellano, R. K. The Influence of Solubilizing Chain Stereochemistry on Small Molecule Photovoltaics. *Adv. Funct. Mater.* **2014**, *24*, 5993−6004.
(14) Liu, J.; Zhang, Y.; Phan, H.; Sharenko, A.; Moonsin, P.; Walker, B.; Promarak, V.; Nguyen, T.-Q. Effects of Stereoisomerism on the Crystallization Behavior and Optoelectrical Properties of Conjugated Molecules. *Adv. Mater.* **2013**, *25*, 3645−3650.
(15) Grenier, C. R. G.; George, S. J.; Joncheray, T. J.; Meijer, E. W.; Reynolds, J. R. Chiral Ethylhexyl Substituents for Optically Active Aggregates of Π-Conjugated Polymers. *J. Am. Chem. Soc.* **2007**, *129*, 10694−10699.
(16) Lee, J. S.; Son, S. K.; Song, S.; Kim, H.; Lee, D. R.; Kim, K.; Ko, M. J.; Choi, D. H.; Kim, B.; Cho, J. H. Importance of Solubilizing Group and Backbone Planarity in Low Band Gap Polymers for High Performance Ambipolar Field-Effect Transistors. *Chem. Mater.* **2012**, *24*, 1316−1323.
(17) Rivnay, J.; Mannsfeld, S. C. B.; Miller, C. E.; Salleo, A.; Toney, M. F. Quantitative Determination of Organic Semiconductor Microstructure from the Molecular to Device Scale. *Chem. Rev.* **2012**, *112*, 5488−5519.
(18) Tummala, N. R.; Elroby, S. A.; Aziz, S. G.; Risko, C.; Coropceanu, V.; Brédas, J.-L. Packing and Disorder in Substituted Fullerenes. *J. Phys. Chem. C* **2016**, *120*, 17242−17250.
(19) Kumar, P.; Shivananda, K. N.; Zajączkowski, W.; Pisula, W.; Eichen, Y.; Tessler, N. The Relation between Molecular Packing or Morphology and Chemical Structure or Processing Conditions: The Effect on Electronic Properties. *Adv. Funct. Mater.* **2014**, *24*, 2530−2536.
(20) Niazi, M. R. Solution-Printed Organic Semiconductor Blends Exhibiting Transport Properties on Par with Single Crystals. *Nat. Commun.* **2015**, *6*, 8598.
(21) Smith, J.; Zhang, W.; Sougrat, R.; Zhao, K.; Li, R.; Cha, D.; Amassian, A.; Heeney, M.; McCulloch, I.; Anthopoulos, T. D. Solution-Processed Small Molecule-Polymer Blend Organic Thin-Film Transistors with Hole Mobility Greater Than 5 Cm2/Vs. *Adv. Mater.* **2012**, *24*, 2441−2446.
(22) Deng, X.; Zheng, L.; Yang, C.; Li, Y.; Yu, G.; Cao, Y. Polymer Photovoltaic Devices Fabricated with Blend Mehppv and Organic Small Molecules. *J. Phys. Chem. B* **2004**, *108*, 3451−3456.
(23) Guo, X.; Watson, M. D. Conjugated Polymers from Naphthalene Bisimide. *Org. Lett.* **2008**, *10*, 5333−5336.
(24) Effenberger, F.; Endtner, J. M.; Miehlich, B.; Münter, J. S. R.; Vollmer, M. S. Synthesis of Anthryl-Substituted Bithienylpyridines and Their N-Methylpyridinium Salts. *Synthesis* **2000**, *2000*, 1229−1236.
(25) Proehl, H.; Dienel, T.; Nitsche, R.; Fritz, T. Formation of Solid-State Excitons in Ultrathin Crystalline Films of Ptcda: From Single Molecules to Molecular Stacks. *Phys. Rev. Lett.* **2004**, *93*, 097403.
(26) Shi, M.-M.; Chen, Y.; Nan, Y.-X.; Ling, J.; Zuo, L.-J.; Qiu, W.-M.; Wang, M.; Chen, H.-Z. Π−Π Interaction among Violanthrone Molecules: Observation, Enhancement, and Resulting Charge Transport Properties. *J. Phys. Chem. B* **2011**, *115*, 618−623.
(27) Tanaka, S.; Miyata, K.; Sugimoto, T.; Watanabe, K.; Uemura, T.; Takeya, J.; Matsumoto, Y. Enhancement of the Exciton Coherence Size in Organic Semiconductor by Alkyl Chain Substitution. *J. Phys. Chem. C* **2016**, *120*, 7941−7948.
(28) Fong, H. H.; So, S. K.; Sham, W. Y.; Lo, C. F.; Wu, Y. S.; Chen, C. H. Effects of Tertiary Butyl Substitution on the Charge Transporting Properties of Rubrene-Based Films. *Chem. Phys.* **2004**, *298*, 119−123.
(29) Käfer, D.; Ruppel, L.; Witte, G.; Wöll, C. Role of Molecular Conformations in Rubrene Thin Film Growth. *Phys. Rev. Lett.* **2005**, *95*, 166602.
(30) Park, S.-W.; Choi, J.-M.; Lee, K. H.; Yeom, H. W.; Im, S.; Lee, Y. K. Amorphous-to-Crystalline Phase Transformation of Thin Film Rubrene. *J. Phys. Chem. B* **2010**, *114*, 5661−5665.
(31) Bergantin, S.; Moret, M. Rubrene Polymorphs and Derivatives: The Effect of Chemical Modification on the Crystal Structure. *Cryst. Growth Des.* **2012**, *12*, 6035−6041.
(32) Sundar, V. C.; Zaumseil, J.; Podzorov, V.; Menard, E.; Willett, R. L.; Someya, T.; Gershenson, M. E.; Rogers, J. A. Elastomeric Transistor Stamps: Reversible Probing of Charge Transport in Organic Crystals. *Science* **2004**, *303*, 1644−1646.
(33) Laudise, R. A.; Kloc, C.; Simpkins, P. G.; Siegrist, T. Physical Vapor Growth of Organic Semiconductors. *J. Cryst. Growth* **1998**, *187*, 449−454.
(34) Venables, J. A.; Spiller, G. D. T.; Hanbucken, M. Nucleation and Growth of Thin Films. *Rep. Prog. Phys.* **1984**, *47*, 399−459.
(35) Cataldo, S.; Pignataro, B. Polymeric Thin Films for Organic Electronics: Properties and Adaptive Structures. *Materials* **2013**, *6*, 1159.
(36) Lv, A.; et al. High Mobility, Air Stable, Organic Single Crystal Transistors of an N-Type Diperylene Bisimide. *Adv. Mater.* **2012**, *24*, 2626−2630.
(37) Zhang, Y.; et al. Probing Carrier Transport and Structure-Property Relationship of Highly Ordered Organic Semiconductors at the Two-Dimensional Limit. *Phys. Rev. Lett.* **2016**, *116*, 016602.
(38) Zeng, Y. Q.; Tao, B.; Yin, Z. P. Molecular Orientation Transformation of Pentacene on Amorphous SiO2: A Computational Study on the Initial Growth Stage of Physical Vapor Deposition. *J. Cryst. Growth* **2014**, *405*, 73−80.
(39) Wang, S. D.; Dong, X.; Lee, C. S.; Lee, S. T. Molecular Orientation and Film Morphology of Pentacene on Native Silicon Oxide Surface. *J. Phys. Chem. B* **2005**, *109*, 9892−9896.

DOI: 10.1021/acs.jpcc.6b06175
J. Phys. Chem. C 2016, 120, 23221−23229